

<https://doi.org/10.1038/s41746-024-01128-2>

Multimodal data fusion using sparse canonical correlation analysis and cooperative learning: a COVID-19 cohort study

Check for updates

Ahmet Gorkem Er^{1,2,3} , Daisy Yi Ding⁴, Berrin Er⁵ , Mertcan Uzun³, Mehmet Cakmak⁶, Christoph Sadee¹ , Gamze Durhan⁷, Mustafa Nasuh Ozmen⁷ , Mine Durusu Tanriover⁶, Arzu Topeli⁵, Yesim Aydin Son² , Robert Tibshirani^{4,8}, Serhat Unal³ & Olivier Gevaert^{1,4}

Through technological innovations, patient cohorts can be examined from multiple views with high-dimensional, multiscale biomedical data to classify clinical phenotypes and predict outcomes. Here, we aim to present our approach for analyzing multimodal data using unsupervised and supervised sparse linear methods in a COVID-19 patient cohort. This prospective cohort study of 149 adult patients was conducted in a tertiary care academic center. First, we used sparse canonical correlation analysis (CCA) to identify and quantify relationships across different data modalities, including viral genome sequencing, imaging, clinical data, and laboratory results. Then, we used cooperative learning to predict the clinical outcome of COVID-19 patients: Intensive care unit admission. We show that serum biomarkers representing severe disease and acute phase response correlate with original and wavelet radiomics features in the LLL frequency channel ($cor(Xu_1, Zv_1) = 0.596$, p value < 0.001). Among radiomics features, histogram-based first-order features reporting the skewness, kurtosis, and uniformity have the lowest negative, whereas entropy-related features have the highest positive coefficients. Moreover, unsupervised analysis of clinical data and laboratory results gives insights into distinct clinical phenotypes. Leveraging the availability of global viral genome databases, we demonstrate that the Word2Vec natural language processing model can be used for viral genome encoding. It not only separates major SARS-CoV-2 variants but also allows the preservation of phylogenetic relationships among them. Our quadruple model using Word2Vec encoding achieves better prediction results in the supervised task. The model yields area under the curve (AUC) and accuracy values of 0.87 and 0.77, respectively. Our study illustrates that sparse CCA analysis and cooperative learning are powerful techniques for handling high-dimensional, multimodal data to investigate multivariate associations in unsupervised and supervised tasks.

Coronavirus Disease 2019 (COVID-19), caused by severe acute respiratory syndrome coronavirus 2 (SARS-CoV-2), was declared a pandemic by the World Health Organization (WHO) on March 11, 2020, and has since affected millions of lives worldwide¹. The pandemic has made it clear that even in high-income countries, healthcare services have the potential to be under immense pressure due to overcrowded hospitals and scarce

resources². This has been even more pronounced in areas vital to effective patient management, such as patient prognostication and decisions in emergency triage³.

As it is known, factors like male sex, age, and comorbidities have been tied to disease severity in COVID-19^{4,5}. Anomalies in laboratory results, radiological abnormalities, and the presence of specific viral mutations can

A full list of affiliations appears at the end of the paper. e-mail: ahmetgorkemer@gmail.com; ogevaert@stanford.edu

also influence the clinical course^{6–13}. As a result, since the clinical trajectory of COVID-19 patients varies significantly, addressing this variation becomes crucial in patient management, requiring novel approaches to infer underlying hidden patterns, identify disease phenotypes, and develop models for outcome predictions in real-life settings.

In recent years, the power of multi-modal data fusion in biomedical research has become increasingly evident. Technological innovations allow us to study a patient or a cohort from multiple perspectives using high-dimensional, multiscale biomedical data. Examples of biomedical data include clinical (electronic health records, clinical notes, laboratory results), pathological (histopathology examinations, immunofluorescence staining), molecular (DNA and RNA sequences, transcriptomics, epigenetics), and imaging (X-ray, computed tomography (CT), magnetic resonance imaging (MRI)) data. Machine learning methodologies have been pivotal in combining and analyzing these data modalities, unveiling a myriad of biomarkers that can be harnessed for personalized medicine applications^{14–18}. Pioneer studies in multi-modal data fusion have mainly been developed in oncology: advances in next-generation sequencing, transitioning from conventional histopathology to whole slide imaging, the comprehensive usage of radiological images, and establishing standardized, publicly available large datasets, such as The Cancer Genome Atlas (TCGA), has been a significant catalyst for these studies^{15,19}.

Since a plethora of clinical, laboratory, imaging, and viral genome sequencing data is available for research, COVID-19 offers a promising avenue for applying multi-modal data fusion. However, despite the potential, its application presents unique challenges. Notably, while databases for viral genome sequencing, such as The Global Initiative on Sharing All Influenza Data (GISAID) and The National Center for Biotechnology Information (NCBI), are available, a consolidated approach to link diverse datasets, including imaging, molecular, and clinical information, remains challenging^{20–22}. In addition, implementing data fusion strategies using the data from a real-life patient cohort, without any clinical intervention and standardization, is also compelling.

This paper presents our approach for analyzing multi-modal data in a COVID-19 patient cohort using unsupervised and supervised sparse linear methods. Specifically, we use canonical correlation analysis (CCA) and cooperative learning to understand the relationships between relevant data modalities and predict intensive care unit (ICU) admission, respectively^{23–25}.

Results

Descriptive analysis

In total, 149 patients were enrolled in the study, and 63 patients (42.3%) were admitted to the ICU (Table 1). The mean age was 57.6 ± 16.2 years, and 61 patients (40.9%) were female. Hypertension (48.3%), diabetes mellitus (29.5%), and coronary artery disease (22.1%) were the most common comorbidities. The mean age was higher in the ICU group compared to the non-ICU group (63.9 ± 15.0 vs. 53.1 ± 15.6 , $p < 0.001$). The median CCI was 4 (3–6) in patients hospitalized in ICU compared to 2 (1–4) in those not hospitalized in ICU ($p < 0.001$). Age, sex, comorbidities, and CCI were used as clinical variables in downstream tasks.

The number of patients who underwent chest CT at least once was 127 (Supplementary Fig. 1). In 105 isolated viral genome samples, the number of unique nucleotide mutations was 710, and the number of unique amino acid mutations was 439. The median of nucleotide mutations per strain was 29.0 (21.0–33.0), and the median of amino acid mutations was 22.5 (12.0–27.8) (Supplementary Fig. 2). Fifty-two strains (49.5%) were assigned to Variant 20I (Alpha, V1) according to the Nextclade clades (Fig. 1).

Visualization of the global SARS-CoV-2 strains using Word2Vec embedding

We visualized 300 randomly selected viral strains from each Nextclade clade in the corpus, generated with global viral genome sequences on the GISAID database. This shows that major variants, such as Variants 20I (Alpha, V1), 20H (Beta, V2), 21I, and 21J (Delta's), and Omicron clades, were successfully separated (Fig. 2). Not only separation but also some of

Table 1 | Clinical characteristics of the patients

Variable	ICU (+) (n: 63)	ICU (-) (n: 86)	p value
Age, years, mean (SD)	63.9 (15.0)	53.1 (15.6)	<0.001
Female sex, n (%)	26 (41.3)	35 (40.7)	1
Comorbidities, n (%)			
Hypertension	38 (60.3)	34 (39.6)	0.02
Diabetes mellitus	22 (34.9)	22 (25.6)	0.29
Coronary artery disease	22 (34.9)	11 (12.8)	0.003
Solid organ malignancy	13 (20.6)	19 (22.1)	0.99
Kidney disease	13 (20.6)	10 (11.6)	0.20
Cardiac failure	14 (22.2)	6 (7.0)	0.01
Chronic lung disease	12 (19.0)	7 (8.1)	0.08
Hematologic malignancy	4 (6.3)	7 (8.1)	0.76
Rheumatologic disease	4 (6.3)	3 (3.5)	0.46
Cerebrovascular disease	2 (3.2)	3 (3.5)	1
Peripheral arterial disease	1 (1.6)	1 (1.2)	1
Dementia	2 (3.2)	0 (0.0)	0.18
Liver disease	0 (0.0)	2 (2.3)	0.50
Immunocompromised, n (%)	12 (19.0)	16 (18.6)	1
COVID-19 vaccination history, n (%)	14 (22.2)	8 (9.3)	0.05
Age-adjusted Charlson comorbidity index, median (IQR)	4 (3–6)	2 (1–4)	<0.001
Steroid treatment (Minimum 6 mg/day dexamethasone), n(%)	51 (81.0)	23 (26.7)	<0.001
Hospital LOS, days, median (IQR)	15 (10.5–31.5)	10 (6–14.75)	<0.001
In-hospital mortality, n (%)	19 (30.2)	1 (1.2)	<0.001

ICU intensive care unit, LOS length of stay, IQR interquartile range.

the characteristic features seen in phylogenetic relationships were observed in the embedding space. While more ancestral clades, for instance, Variants 19A, 19B, and 20A, representing the early days of the pandemic, had a wider distribution, clades dating to later periods tend to be observed within clusters. Furthermore, clades that have closer evolutionary relationships, for example, Variants 20H (Beta, V2), 21I (Delta), and 21H (Mu) were located closer in the embedding space²⁶. On the other hand, Omicron variants were separated from these groups, as highlighted in the literature²⁷. It was also seen that some recombinant strains were located close to the Omicron variants, while others tended to spread toward other variants.

Unsupervised pairwise data fusion using sparse CCA

Next, we performed sparse CCA analysis to examine the pairwise associations between all data modalities (Table 2). Relevant sparsity parameters corresponding to the highest Z-stat score were determined with the number of non-zero weights of X and Z. We first report the results for combining laboratory results and radiomics features for 127 patients ($cor(X_{U1}, Z_{V1}) = 0.596$). In the laboratory results group, lactate dehydrogenase (LDH), which relates to disease progression and worse outcome, had the highest coefficient value (0.47), followed by erythrocyte sedimentation rate, D-dimer, polymorphonuclear leukocytes, white blood cell count, and acute phase reactants such as C-reactive protein (CRP) and fibrinogen²⁸. At the same time, albumin had the lowest coefficient value (−0.46) as a negative acute phase reactant, along with hemoglobin, lymphocyte, and sodium levels. In the radiomics features group, original and wavelet features in the LLL frequency channel had the highest absolute values of coefficients. Among them, histogram-based first-order features reporting the skewness, kurtosis, and uniformity had the lowest negative coefficients, whereas entropy-related features had the highest positive coefficients. The negative

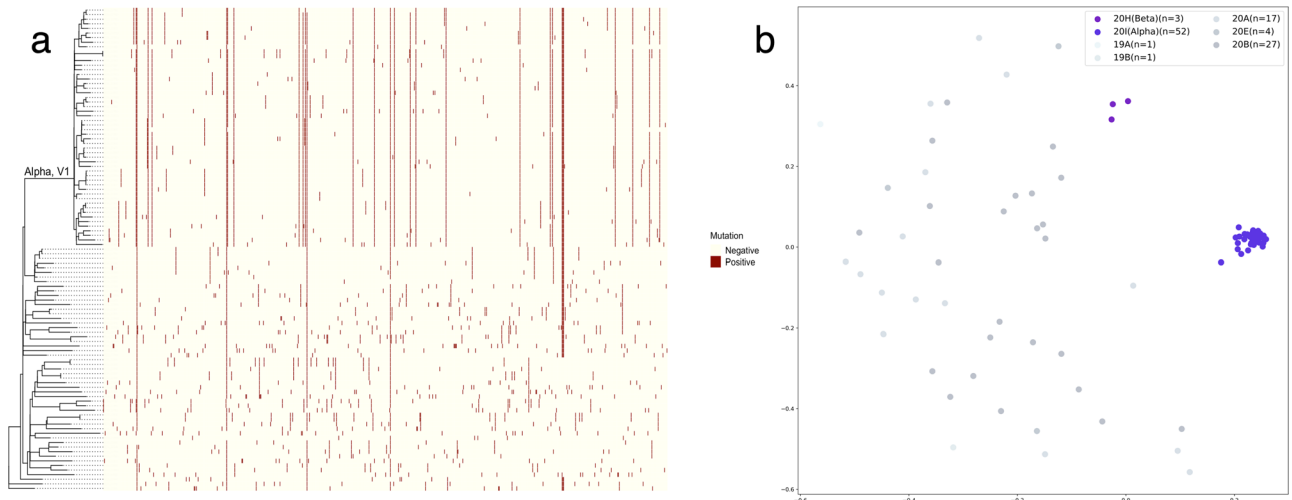


Fig. 1 | Phylogenetic tree, nucleotide substitution matrix, and Word2Vec encoding plot of isolated SARS-CoV-2 strains. **a** The phylogenetic tree of isolated SARS-CoV-2 strains and nucleotide substitutions in matrix form, in which the

presence of substitutions is shown in dark red. **b** The Word2Vec encoding plot of the same strains. The nucleotide substitution matrix and Word2Vec encoding plot represent that Alpha strains appear more similar compared to non-Alpha strains.

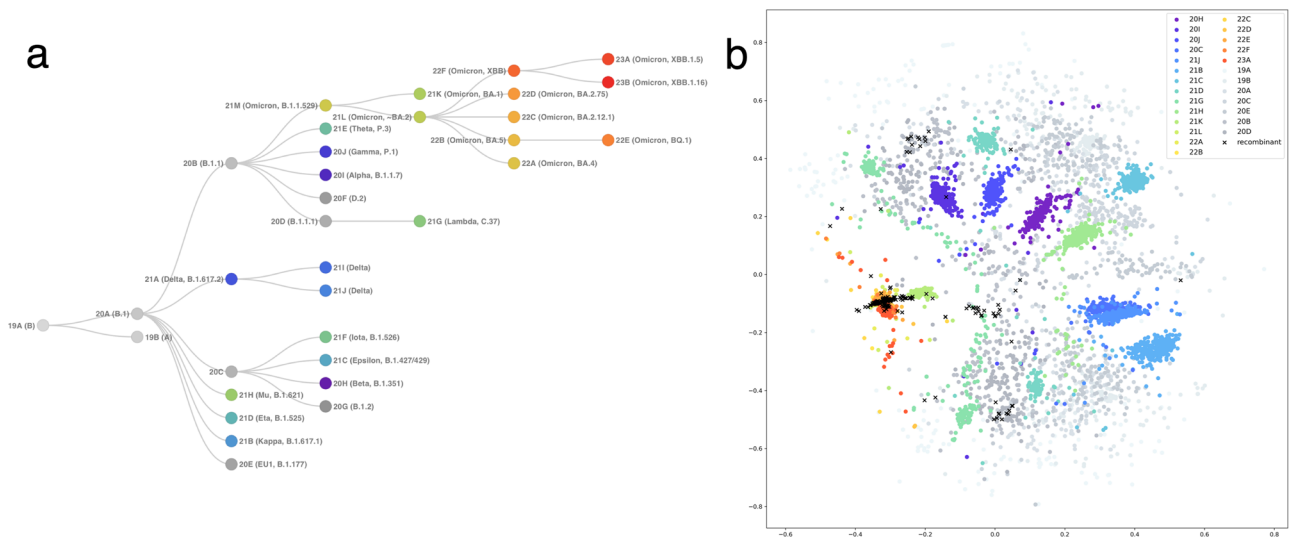


Fig. 2 | Phylogenetic tree and 2D Word2Vec encoding plot of global SARS-CoV-2 strains. **a** The phylogenetic relationships of the global SARS-CoV-2 clades as defined by Nextstrain. The screenshot was taken from CoVariants.org²⁶. **b** the Word2Vec

encoding plot of 300 randomly selected viral strains from each Nextclade clade. Major variants, such as Variants 20I (Alpha, V1), 20H (Beta, V2), 21I, and 21J (Delta's), and Omicron clades, are successfully separated.

coefficients of skewness and kurtosis features indicated that, as laboratory results worsened, since image density is measured approximately as -1000 Hounsfield units (HU) for air, and 0 to $+70$ HU for various tissue types such as blood, pleural effusion, abscess, and mucus, depending on the extent and content of the lung abnormalities, the image intensity histogram became flatter and more right-skewed^{29,30}. This led to a loss of homogeneity and increased entropy in the radiomics features (Fig. 3).

Sparse CCA analysis of laboratory results and clinical data revealed different clinical phenotypes. ($cor(X_{u1}, Z_{v1}) = 0.63$, best L1 bound for X and Z : $0.7, p = 0.04$) (Fig. 4). While laboratory results' first canonical coefficients revealed a phenotype related to high creatinine levels with low albumin levels and anemia, on the clinical side, the patient appeared to be elderly and multi-morbid with moderate to severe renal disease. The second canonical variables represented a different patient phenotype who was young and immunocompromised with high ferritin levels. The third canonical variables also characterized a phenotype that likely presents a patient with a history of liver disease with elevated INR, total bilirubin levels, and hypoalbuminemia.

Next, we focused on the sparse CCA analysis of imaging and clinical data (Supplementary Fig. 3). In this experiment, the permutation-based approach for choosing parameters provided a sparser solution than previous ones; the correlation coefficient was 0.65 ($p < 0.01$). The first and third canonical vectors were found to be associated with sex, and the second and fourth ones were with lymphoma and CCI, respectively. Mainly, the first sex-related canonical vector coefficients belonged to the left, and the second sex-related canonical vector coefficients belonged to the right lung and consisted of first-order and shape radiomics classes. In combinations of pairwise sparse CCA analysis of viral genome sequencing data with other data modalities, different encoding techniques for the viral genome altered the correlation plots, with better separation obtained with Viral-Word2Vec encoding (Supplementary Fig. 4).

Finally, we performed sparse multi-CCA on patients with all data modalities ($n = 89$). When Viral-Binary encoding was used for viral encoding, the highest Z -score was 2.15 (penalties = $12.22, 6.64, 1.56, 1.7, p < 0.01$). The highest Z -score was 3.14 (penalties = $17.923, 8.468, 2.293, 2.493, p < 0.01$) when Viral-Word2Vec was used for viral encoding. We

Table 2 | Sparse CCA analysis for examining pairwise associations between all data modalities

Data modalities		<i>n</i>	Best L1 bound for <i>X</i> and <i>Z</i>	Z-stat	<i>p</i> value	Number of non-zero weights		Correlation
Radiomics	Lab Results	127	0.70/0.70	2.882	<0.01	1199	17	0.596
Radiomics	Clinical Data	127	0.10/0.10	3.423	<0.01	26	1	0.646
Radiomics	Viral-Binary E.	89	0.50/0.50	0.558	0.16	462	235	0.761
Radiomics	Viral-Word2Vec E.	89	0.70/0.70	0.584	0.20	775	241	0.524
Lab Results	Clinical Data	127	0.70/0.70	1.392	0.04	16	21	0.628
Lab Results	Viral-Binary E.	89	0.23/0.23	1.012	0.24	2	201	0.915
Lab Results	Viral-Word2Vec E.	89	0.10/0.10	0.489	0.20	1	6	0.576
Clinical Data	Viral-Binary E.	105	0.3/0.3	3.281	<0.01	17	328	0.982
Clinical Data	Viral-Word2Vec E.	105	0.7/0.7	0.214	0.36	20	206	0.487

Sparsity parameters and correlations were calculated with the CCA.permute function. We chose the L1 bound for *X* and *Z* at the highest value of the Z-stat for each pairwise data modality. *n* number, *E* encoding.

showed that with the Viral-Word2Vec embedding, the viral genome projection of the patients was more homogeneously distributed, and pairwise correlation values of viral features and other data modalities were reduced (Fig. 5). While the dominance of histogram-based first-order radiomics features and the importance of albumin and LDH among the laboratory results persisted in the analysis of these 89 patients, clinical data's first canonical vectors slightly revealed a different clinical phenotype which was an elderly multimorbid patient with dementia (Supplementary Fig. 5).

Supervised multiview analysis using cooperative learning

We performed cooperative learning to build prediction models for ICU admission. First, we used all five data modalities to train unimodal prediction models in all patients. The highest score was achieved with the model using radiomics features (AUC = 0.83 ± 0.01), followed by laboratory results and clinical data (AUC = 0.77 ± 0.02 vs. 0.67 ± 0.02), respectively (Supplementary Table 1 and Supplementary Fig. 6).

Then, the models were trained with all available singular, dual, and quad data combinations and evaluated for the same task in 89 patients. The best accuracy and AUC values were achieved with the quadruple model, which combines clinical, laboratory, radiomics, and viral genome sequencing data using Viral-Word2Vec encoding (CLRW) (Supplementary Table 2 and Fig. 6). While unimodal prediction models of radiomics features and laboratory results had a mean AUC score of 0.83, the quadruple prediction model using Viral-Word2Vec encoding achieved a mean AUC score of 0.87. The mean AUC score for the quadruple model using Viral-Binary encoding was 0.83 ± 0.2. There was a statistical difference between these two quadruple models ($p < 0.001$). The model that combines radiomics and Viral-Word2Vec encoding also outperformed the model that combines radiomics and Viral-Binary encoding in terms of AUC scores (0.86 vs. 0.83, $p < 0.001$). There was no statistical difference when we used different viral embedding techniques in other models with dual data combinations.

To understand which features were the most important for the performance of the CLRW model, we used all the available data as the training set. We performed a 5-fold CV to get the optimal hyperparameters and found Alpha and rho as 0.2 and 0.1, respectively. Model standardized coefficients were extracted at $\lambda = 0.1$ (Supplementary Fig. 7). Again, like the results of the unsupervised sparse CCC analysis of radiomics and laboratory results, the original and wavelet features in the LLL frequency channel had the highest absolute values for the standardized coefficients. LDH, ESR, CRP, albumin, and total bilirubin were the selected serum biomarkers, and age, chronic disease, and CCI were the clinical variables of the CLRW model. Word2Vec encoding also contributed to the supervised task with its 4 out of 300 dimensions.

Discussion

The complexities of modern biomedical challenges demand more holistic approaches to data analysis. This study spotlights the potential of multi-

modal data fusion, harnessing diverse data modalities to derive deeper insights into health phenomena. By integrating disparate data types, we can uncover nuanced patterns and relationships that single-modal analyses might miss. In particular, the potential of integrating viral genome sequencing, imaging, clinical data, and laboratory results is immense. Sparse CCA analysis and cooperative learning, as highlighted in our study, are instrumental in combining these data strands, offering a multi-faceted view of a complex disease such as COVID-19. Our exploration into using the Word2Vec NLP model for viral embedding further underscores the value of innovative techniques in transforming raw data into meaningful representations, especially in the context of viral genomic sequencing data.

Our approach has precedence. Using NLP techniques, particularly the Word2Vec model for viral embedding, has been recognized in prior research. But while earlier studies were often unimodal and focused on tasks like viral classification or evolution tracking, our method differs by integrating this with other data modalities, offering a more comprehensive view^{31–34}. The merit of this method is evident in its ability to encapsulate the cumulative effects of multiple viral mutations and their relationships, a task that single-modal approaches might find challenging. For example, we illustrated that Word2Vec encoding not only separates major SARS-CoV-2 variants but also allows the preservation of phylogenetic relationships among them. We also found that Word2Vec encoding is beneficial in showing which groups recombinant strains are close to, which might be challenging to represent in a phylogenetic tree.

Next, imaging data, particularly CT scans, holds potentially more information than can be observed by radiologists. Radiomics offers a quantitative approach to interpreting this data, allowing correlations with clinical features and laboratory results. Previous literature has highlighted the correlation between radiological findings and other biomarkers^{35–37}. Our analysis shows that serum biomarkers that represent positive and negative acute phase responses are mainly found to be correlated with radiomics features related to the distribution of voxel intensities. As known, in lung nodule and cancer studies, mainly shape-related features are robust and provide information about disease phenotypes and prognosis; however, our results emphasize the importance of histogram- and entropy-related features because a higher proportion of involved lung parenchyma, i.e., diffuse pulmonary infiltrates, is associated with severe disease^{38–40}. Furthermore, we reveal that biomarkers not playing a role in acute phase response, such as ALT, potassium, and creatinine, are not correlated with radiomics features.

Sparse CCA has been championed in various biomedical domains, from understanding eating disorders via imaging data to categorizing clinical subtypes in dementia^{41,42}. Our application to COVID-19 aligns with this trajectory, delineating clinical phenotypes like kidney disease, liver dysfunction, and age-related vulnerabilities, supported by existing literature and our clinical observations^{43–46}. However, challenges persist. Multi-modal data fusion demands rigorous computational techniques, nuanced strategies for feature extraction, and the transformation of raw data into a structured

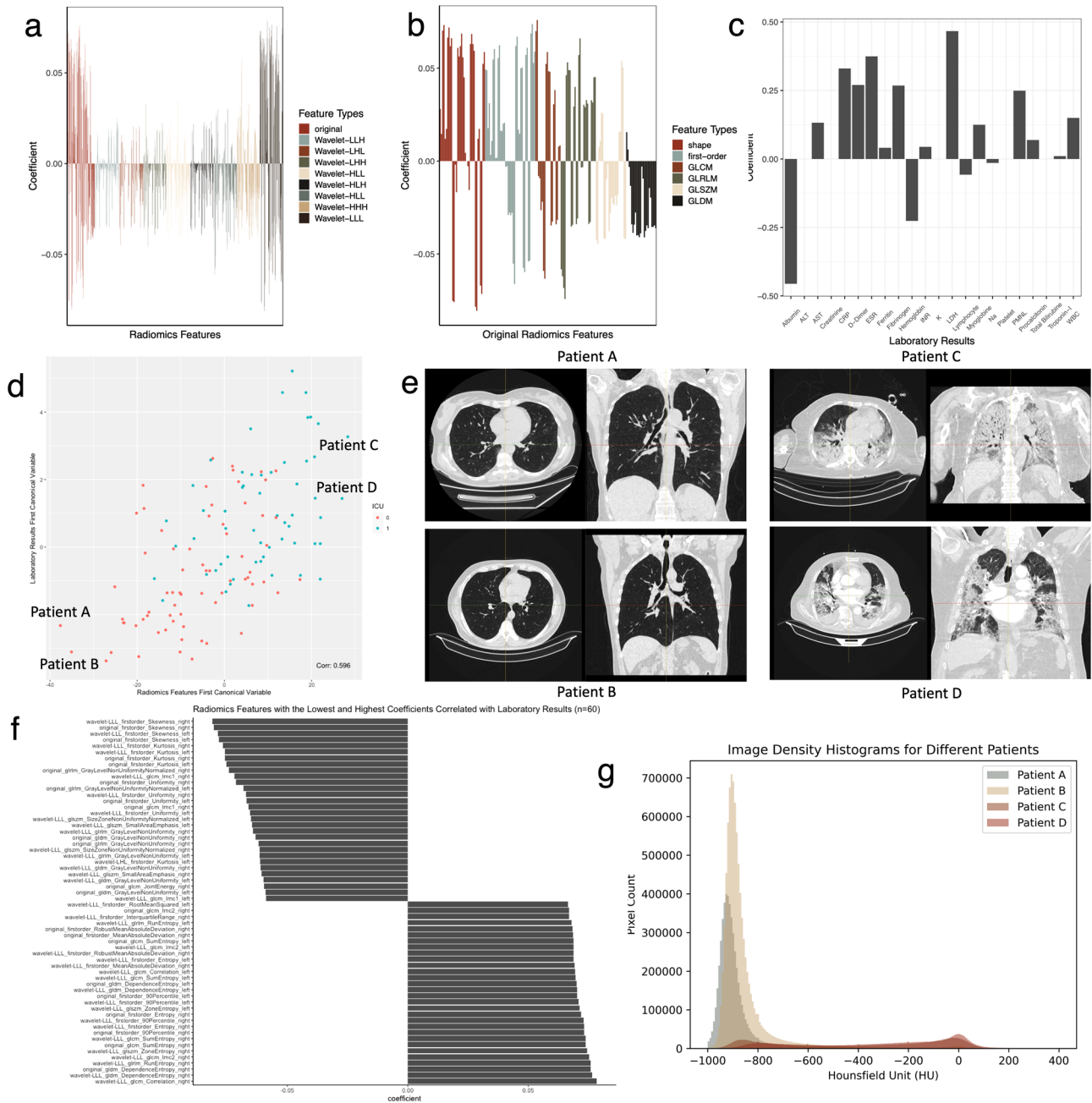


Fig. 3 | Sparse CCA analysis of radiomics features and laboratory results.
a Correlated radiomics features. Original and wavelet features in the LLL frequency channel have the highest absolute values of coefficients. **b** Coefficients of the original radiomics features. **c** Correlated laboratory results. Coefficients of laboratory results align with serum biomarkers related to severe disease and acute phase response. **d** The correlation between the first set of canonical variables shows that the first pair can capture the ICU outcome. We select two patients (Patient A and Patient B) with the lowest and two patients (Patient C and Patient D) with the highest canonical variables for radiomics features. **e** Patient A and Patient B’s CT images in axial and

coronal planes have no pulmonary infiltration, whereas there are apparent findings on Patient C and Patient D’s CT images for COVID-19 pneumonia. **f** We select and visualize 30 variables with the highest and 30 variables with the lowest coefficients among the radiomics features. **g** The image intensity histograms of the patients show that Patient A and Patient B have left-skewed histograms peaking around -1000 HU, consistent with air and lung parenchyma densities; however, histograms of Patient C and Patient D are flatter and more right-skewed, consistent with negative coefficients for skewness and kurtosis features and revealing a wider distribution of HU values.

format. Our experiments show that when these elements align—as seen with the optimal results using Word2Vec encoding—the outcomes are promising. This performance edge over Viral-Binary encoding likely arises because Word2Vec benefits from an expansive external database, capturing nuances not specific to our dataset.

There are various studies focusing on predicting a supervised task by combining imaging and clinical data in COVID-19 patients^{36,47–51}. It is foreseeable that viral genome sequencing will be directly integrated into

clinical patient management in the coming years⁵². Yet, decisions surrounding data fusion techniques and staging remain paramount. We employed cooperative learning, enhancing alignment across modalities, to determine optimal fusion, guided by the agreement penalty tuning to distinguish which patients should be admitted to the medical ward or ICU when the relevant patient data was collected. At the end of the analysis, a review of the features selected in both our unsupervised and supervised models revealed a consistency, highlighting a harmony between an

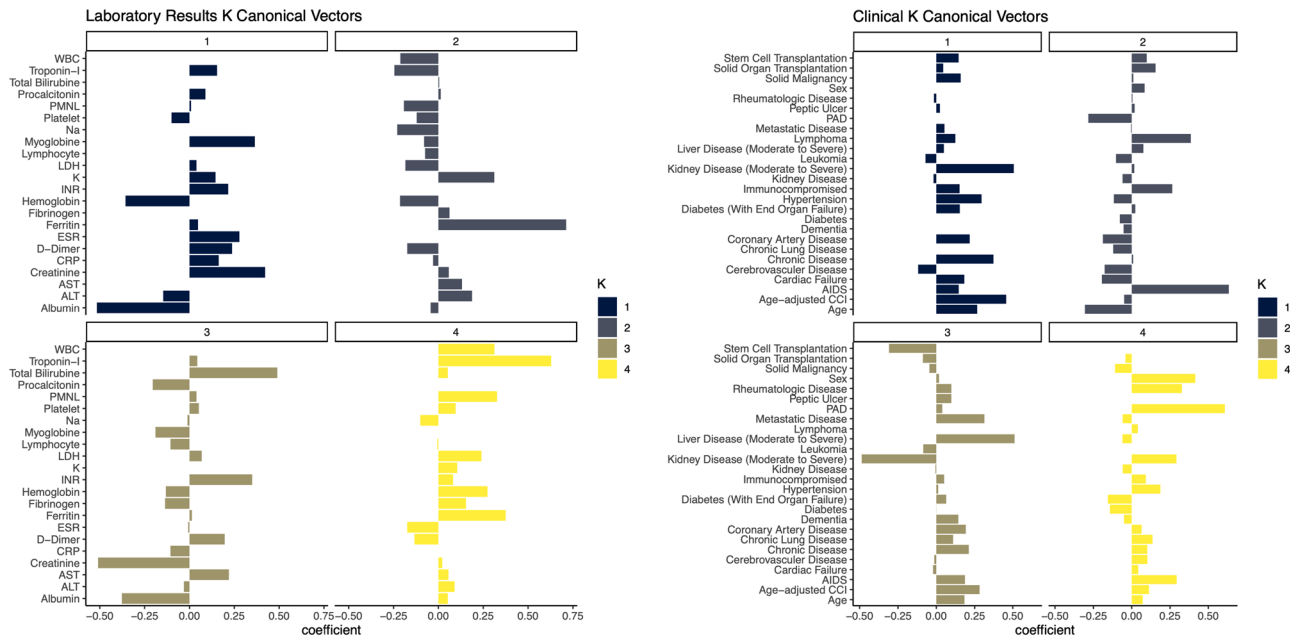


Fig. 4 | Sparse CCA analysis of laboratory results and clinical data. The first four canonical variables are provided. Different canonical variables provide different clinical phenotypes: the first canonical variables represent a patient phenotype who is elderly, multi-morbid, and has moderate to severe renal disease with high

creatinine and myoglobin levels, whereas the third canonical variables represent a different patient phenotype with moderate to severe liver disease with high bilirubin and INR levels.

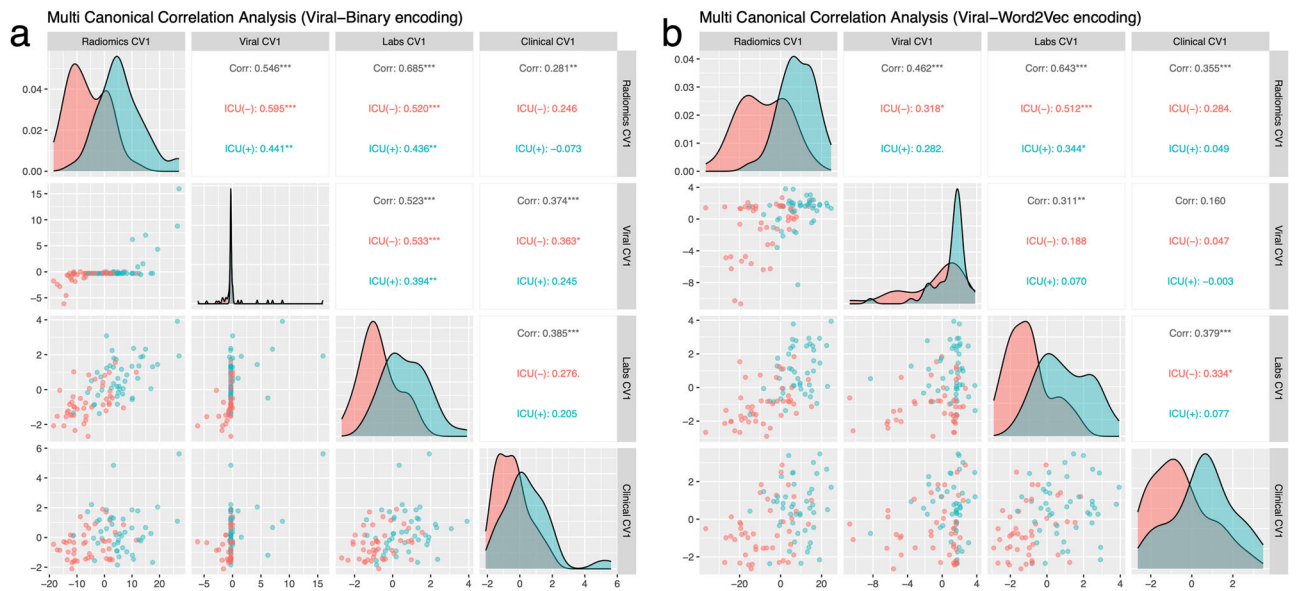


Fig. 5 | Sparse multi-CCA analysis of all data modalities. **a** The correlation pairs plot of the first canonical vectors of four data modalities, including Viral-Binary encoding. **b** Using Viral-Word2Vec encoding instead of Viral-Binary encoding provides a more homogenous distribution and better separation among canonical variables.

unsupervised use of sparse CCA analysis and supervised predictive cooperative learning.

A few caveats need to be noted. First, our relatively small sample size might be suffering from overfitting of data. To overcome this issue, we used a stratified nested CV framework for estimating the generalization performances of the trained models. The sparsity penalty in both sparse CCA and cooperative learning also helped mitigate the risk of overfitting. Next, from a clinical point of view, this study is dated in the early days of the pandemic, and a small number of patients were vaccinated for COVID-19. Because it is not possible to quantify the vaccination effect properly, we had to ignore this effect.

To conclude, our findings reinforce the power and potential of multi-modal data fusion in biomedical research. Sparse CCA analysis and cooperative learning are pivotal tools in managing and interpreting high-dimensional data, as in the example of COVID-19. The Word2Vec model, as employed for viral genome encoding, is particularly promising, hinting at future directions for research in multi-modal biomedical data fusion.

Methods

Study design and data collection

This prospective cohort study was conducted in a tertiary care academic center in Ankara, Turkey, between December 22, 2020, and May 5, 2021.

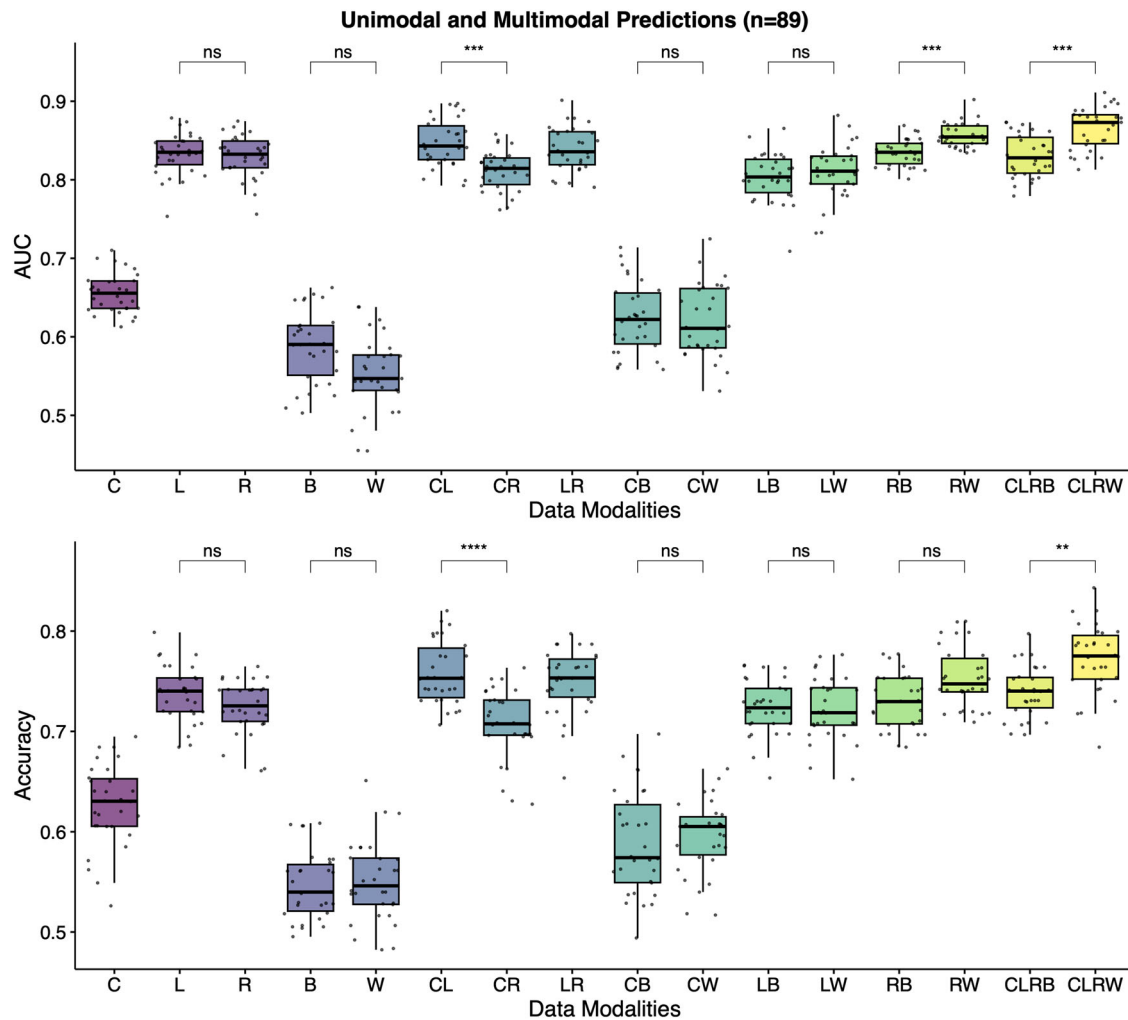


Fig. 6 | Unimodal and multimodal prediction models for the supervised task. The best accuracy and AUC values are achieved with the quadruple model using Word2Vec Encoding (CLRW). C clinical data, L laboratory results, R radiomics, B viral-binary encoding, W Viral-Word2Vec encoding, AUC area under the curve, ns non-significant.

The cohort consisted of two groups of patients: one group recruited as a part of the project entitled “Viral Genome Analysis in COVID-19 Patients and Genotyping of Genetic Variants Shown in the Literature Related to the Severe Course of the Disease in Humans” and the other group recruited within the scope of the Global Influenza Hospital Surveillance Network Project (GIHSN)-2020-21 in Turkey⁵³. Ethical approvals were obtained from the Institutional Ethics Committee with the code numbers GO 2021/02-22, GO 20-102, and GO 22-1211. Good clinical and laboratory practices were followed throughout the study in accordance with the Declaration of Helsinki.

Adult patients (≥18 years of age) hospitalized in the medical wards or intensive care units (ICU) who were positive for SARS-CoV-2 polymerase chain reaction (PCR) test within the last 120 h and gave written informed consent were included in the study. COVID-19 patients with at least one of the below criteria were admitted to the ICU:

- Dyspnea and respiratory distress,
- Respiratory rate >30/min,
- PaO₂/FiO₂ < 300 mmHg,
- Increased oxygen demand during follow-up,
- SpO₂ < 90% or PO₂ < 70 mmHg despite 5 l/min O₂ support,
- Hypotension (Systolic blood pressure <90 mmHg or more than 40 mmHg drop from usual systolic blood pressure level or mean arterial blood pressure <65 mmHg),
- Development of acute organ dysfunction such as acute kidney injury, acute elevation in liver function tests, confusion, acute bleeding diathesis,

- Elevated serum troponin with arrhythmia,
- Lactate >2 mmol/l.

Relevant clinical information was gathered through face-to-face interviews with patients and attending physicians and by reviewing clinical records. Age, sex, comorbidities such as diabetes, heart failure, coronary artery disease, hypertension, malignancy, polymerase chain reaction (PCR) test results, vaccination history, medications and therapies, outcomes, laboratory results, GISAID EPI_SET identifiers, and imaging data were recorded. Age-adjusted Charlson comorbidity index (CCI) was calculated for each patient. Min-max normalization was performed for age and CCI. Since laboratory results can change within days or even hours in COVID-19 patients, only results at the time of imaging were included. Among recorded 22 laboratory features out of 127 patients, erythrocyte sedimentation rate (ESR) was missing in 5 (4%), and troponin-I and myoglobin were absent in 11 (8.7%) patients. The mean substitution was performed to handle these missing values. All the information related to patients has been anonymized.

Sampling and next-generation viral genome sequencing protocol

A nasopharyngeal swab or nasal specimen combined with an oropharyngeal swab was obtained from conscious patients, and a tracheal aspirate from intubated patients, in case they comply with inclusion criteria. Medical Wire M40-A Compliant Sigma-Virocult™ Viral Collection and Transport System combining open-bud Sigma-Swab™ with Virocult™ medium was used. EZ1

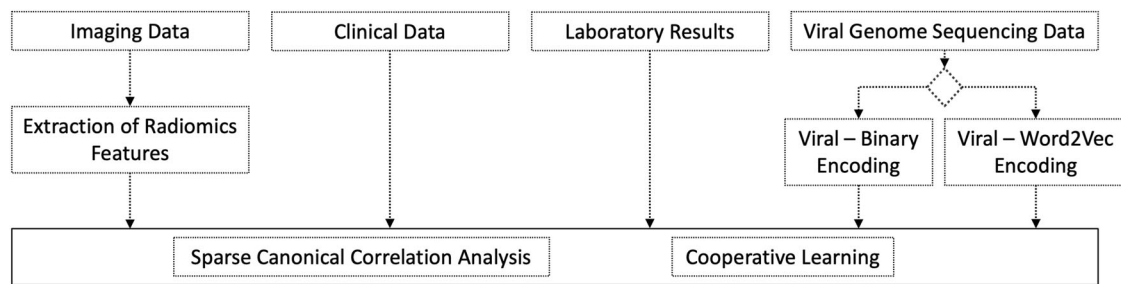


Fig. 7 | Flowchart of the methods used in the study. Unsupervised sparse canonical correlation analysis and supervised cooperative learning are used for multi-modal data fusion. Two different viral encoding techniques are performed and compared in these analyses.

Virus mini kit V2.0 (Catalog number: 955134, Qiagen, Germany) was used for total nucleic acid extraction. Samples were directly introduced to the sequencing platform after nucleic acid extraction. Library preparation was performed using Respiratory Virus Oligos Panel V2 (Illumina Inc., #20044311) and Illumina RNA Prep with Enrichment, (L) Tagmentation (Illumina Inc., #20040537) kits according to official protocol. Before sequencing, the libraries were quantified and checked on Qubit 4 Fluorometer (ThermoFisher Inc.) and 2100 Bioanalyzer systems (Agilent Inc.). The sequencing was performed on Illumina NextSeq 550 platforms with 1,000,000 reads (2×150 bp) per sample on average. Quality control of the raw data was analyzed using the FASTQC tool. The quality passed samples were uploaded to BaseSpace (Illumina Inc.) for bioinformatics analysis. The data were analyzed using the DRAGEN COVID Lineage app (v.3.5.4) on the BaseSpace platform. The low-quality and low-variant fraction variants were filtered out (coverage >10). The filtered variants were submitted to the GISAID database²⁰.

Identifying viral mutations and construction of phylogenetic tree

Viral genome sequences were retrieved from the GISAID database (Supplementary Note 1). Nextclade CLI (v.2.12.0) was used for sequence alignment and identifying the nucleotide and amino acid mutations and variant clades⁵⁴. The reference genome was determined as SARS-CoV-2 isolate Wuhan-Hu-1, GenBank: MN908947.3. Isolated study strains' phylogenetic tree construction was performed using an optimized substitution model (GTR + F + I) according to the lowest Bayesian Information Criterion (BIC) score obtained by the ModelFinder approach and followed by ultrafast bootstrap analysis (175 iterations) on the IQ-TREE software (v.1.6.12)^{55–57}. Consensus tree annotation and visualization were then completed using the ggtree (v.3.8.0) R package⁵⁸.

Our approach contained the following steps (Fig. 7):

- Using binary encoding and leveraging the Word2vec natural language processing model (NLP) for viral encoding⁵⁹.
- Extraction of radiomics features from CT images.
- Performing canonical correlation analysis to understand relationships between data modalities and identify clinical phenotypes^{23,24}.
- Using cooperative learning to build prediction models for ICU admission²⁵.

Viral feature preprocessing

Before utilizing any machine learning model on a genome or amino acid sequence, it is necessary to convert the sequence into a numerical format of fixed length to construct an embedding space. For this purpose, various techniques available in the literature are broadly classified as alignment-free and alignment-based methods⁶⁰. Alignment-free methods are mainly divided into word-based and information theory-based methods. While word-based methods rely on discovering the frequency of words (k-mers) within sequences and use similarity or dissimilarity measures derived from these patterns, information theory-based methods capture the information shared among sequences using entropy or complexity metrics⁶¹. On the other hand, even though alignment-based methods have some disadvantages, such as becoming computationally expensive or assuming that

homologous sequences share conserved sequences, they still constitute a well-established approach in phylogenetic studies. During the COVID-19 pandemic, Pango, Nextclade, and WHO classification systems have been widely used, and all these systems essentially rely on this methodology^{62,63}. Also, they were used in machine-learning prediction studies for creating viral feature embeddings^{64,65}.

We tried and compared two different techniques for viral encoding:

- Viral-Binary encoding: as a typical example of alignment-based methods, according to whether mutations were present or were not, each mutation was encoded as “0” or “1”. In total, 439 unique amino acid mutations were identified in 105 isolated study strains. This created a binary column for each mutation and returned a sparse matrix.
- Viral-Word2Vec encoding: since well-established viral genome databases exist on a global scale, we aimed to combine alignment-free and alignment-based models leveraging the Word2Vec NLP model to reduce the size of the embedding space and extract the semantic relationship between each of the mutations and the strains themselves^{59,66}. We treated amino acid mutations as words and strains as sentences and used the Skip-Gram model architecture that predicts surrounding mutations in a context window given the current mutation. To construct the corpus, viral strains whose outcomes were known and collected between December 30, 2019, and March 2, 2023, on the GISAID database were used. After collecting the data, we defined the outlier strains as falling below $Q1 - 1.5$ IQR or above $Q3 + 1.5$ IQR in terms of the number of mutations. As a result, 653,134 viral genomes were used for constructing the corpus. The maximum number of mutations per strain was found to be 115, and accordingly, this number was chosen as the context window to train the Word2Vec model with vector dimension 300. The vocabulary size (the number of unique amino acid mutations) was found to be 52,311. Strain embeddings were calculated by getting the strains' mean vector of amino acid mutations. Multi-dimensional scaling (MDS) was used to reduce dimensionality and visualize 2D plots⁶⁷. Cosine similarities between the strains were computed to construct a dissimilarity matrix, and this matrix was used as the precomputed dissimilarity metric in MDS.

Imaging data collection and analysis

For each patient with longitudinal CT images, the images were selected based on the following criterion: Since the study outcome for the supervised task is discharge from the medical ward (non-ICU group) or ICU admission (ICU group), we selected images closest to the outcome (Supplementary Fig. 8). Image data were obtained from SIEMENS scanners. CT section thickness was as follows: less than 1 mm (7 patients, 5.5%), greater than or equal to 1, less than 2 mm (119 patients, 93.7%), and greater than or equal to 2 mm, less than 3 mm (1 patient, 0.01%). All images were visualized in 3D Slicer (v.5.3.0), and the right and left lungs were segmented with U-net-based pre-trained lungmask R231^{68,69}. Eighteen first-order, 14 shape, 22 Gray-level co-occurrence matrix (GLCM), 16 Gray-level size zone matrix (GLSZM), and 14 Gray-level dependence matrix (GLDM) features were extracted from

original and wavelet-filtered images from each lung using pyradiomics (v.3.0.1)⁷⁰. All images were normalized with a scale of 500. “sitkBSpline” was used as the interpolator for resampling pixel space to (1.0,1.0,1.0) mm. A fixed bin number of 64 was used for all analyses.

Data fusion methodologies

Assume we have two data matrices, X and Z , of dimensions $n \times p$ and $n \times q$ on the same set of n observations are given as Eq. (1):

$$X = \begin{bmatrix} x_{11} & x_{12} & \cdots & x_{1p} \\ x_{21} & x_{22} & \cdots & x_{2p} \\ \vdots & \vdots & \ddots & \vdots \\ x_{n1} & x_{n2} & \cdots & x_{np} \end{bmatrix} \quad Z = \begin{bmatrix} z_{11} & z_{12} & \cdots & z_{1q} \\ z_{21} & z_{22} & \cdots & z_{2q} \\ \vdots & \vdots & \ddots & \vdots \\ z_{n1} & z_{n2} & \cdots & z_{nq} \end{bmatrix} \quad (1)$$

Canonical correlation analysis (CCA) seeks linear combinations (canonical variables) of the variables in X and Z that are maximally correlated. That is, $u_1 = (u_{11}, u_{21}, \dots, u_{p1})^T$ and $v_1 = (v_{11}, v_{21}, \dots, v_{q1})^T$ maximize $\text{corr}(Xu_1, Zv_1)$. Here, we refer to u_1 and v_1 as the canonical vectors and Xu_1 and Zv_1 as the canonical variables. u and v have the dimensions of $p \times K$ and $q \times K$ for K canonical vectors, which are not correlated with each other.

Sparse CCA aims to find sparse canonical vectors u and v such that $u^T X^T Z v$ is optimized. The analysis was conducted using the PMA (v.1.2.1) package²⁴, where we used the CCA.permute function for selecting the sparsity parameters. Multi-CCA was used as an extension where we assessed the relationship between more than two data modalities. The p values were calculated through permutation with the MultiCCA.permute function.

Cooperative learning was used for the supervised learning task to build prediction models for ICU admission with multimodal data, which uses an agreement penalty to encourage alignment between predictions from different data modalities. By varying the weight of the agreement penalty, it provides a continuum of solutions that include the early and late fusion approaches. Using cross-validation (CV), we chose the degree of agreement, i.e., the optimal weight on the agreement penalty. Cooperative learning also combines the lasso penalty with the agreement penalty, yielding feature sparsity. Analyses were performed with the multiview (v.0.8) package²⁵.

We used a repeated stratified nested CV framework for hyperparameter tuning, model selection, and assessment (Supplementary Fig. 9). Ten-fold CV was performed, with the loss function as “deviance” for tuning the elastic-net mixing parameter and the weight of the agreement penalty in the inner loop. The outer loop assessed the performance of models trained in the inner loop. The final performance scores were averaged after a 5-fold CV. We conducted each experiment 30 times.

Statistical analysis

Descriptive statistics were used to calculate frequency and percent distributions. After testing assumptions of normality, the mean and standard deviation were used for continuous variables with normal distribution and the median and interquartile range for continuous variables without normal distribution. The statistical significance of the differences between groups was tested using Chi-square and Fischer’s exact Chi-square tests for categorical variables, an independent two-sided t -test for continuous variables with normal distribution, and a Mann–Whitney U test for continuous variables without normal distribution. The equality of variances of the results of cooperative learning was assessed with Bartlett’s test. If the hypothesis of equal variances was rejected, Welch’s ANOVA was used to test the significance between three or more groups. The Games-Howell post hoc test was used as the nonparametric approach to compare pairwise results of cooperative learning. Type I error was set at 0.05 for all analyses.

Reporting summary

Further information on research design is available in the Nature Research Reporting Summary linked to this article.

Data availability

The data supporting this study’s findings are available on request from the corresponding authors. The data are not publicly available due to privacy or ethical restrictions. All genome sequences used for training the Word2Vec NLP model and associated metadata in this dataset are published in GISAID’s EpiCoV database. To view the contributors of each individual sequence with details such as accession number, virus name, collection date, originating lab and submitting lab, and the list of authors, visit <https://doi.org/10.55876/gis8.231104eq>.

Code availability

The code used for the analysis is available on a GitHub repository at https://github.com/ahmetgorkemer/multimodal_covid19_study.

Received: 6 November 2023; Accepted: 25 April 2024;

Published online: 07 May 2024

References

- World Health Organization. *Coronavirus Disease 2019 (COVID-19): Situation Report*, 51 (World Health Organization, 2020).
- El Bcheraoui, C., Weishaar, H., Pozo-Martin, F. & Hanefeld, J. Assessing COVID-19 through the lens of health systems’ preparedness: time for a change. *Glob. Health* **16**, 112 (2020).
- Wu, L. & Kong, X. COVID-19 pandemic: ethical issues and recommendations for emergency triage. *Front. Public Health* **11**, 1160769 (2023).
- Williamson, E. J. et al. Factors associated with COVID-19-related death using OpenSAFELY. *Nature* **584**, 430–436 (2020).
- Petrilli, C. M. et al. Factors associated with hospital admission and critical illness among 5279 people with coronavirus disease 2019 in New York City: prospective cohort study. *BMJ* **369**, m1966 (2020).
- Wu, C. et al. Risk factors associated with acute respiratory distress syndrome and death in patients with coronavirus disease 2019 pneumonia in Wuhan, China. *JAMA Intern. Med.* **180**, 934–943 (2020).
- Kwee, T. C. & Kwee, R. M. Chest CT in COVID-19: what the radiologist needs to know. *RadioGraphics* **40**, 1848–1865 (2020).
- Liao, D. et al. Haematological characteristics and risk factors in the classification and prognosis evaluation of COVID-19: a retrospective cohort study. *Lancet Haematol.* **7**, e671–e678 (2020).
- Bao, C., Liu, X., Zhang, H., Li, Y. & Liu, J. Coronavirus disease 2019 (COVID-19) CT findings: a systematic review and meta-analysis. *J. Am. Coll. Radiol.* **17**, 701–709 (2020).
- Flores-Vega, V. R. et al. SARS-CoV-2: evolution and emergence of new viral variants. *Viruses* **14**, 653 (2022).
- Young, B. E. et al. Effects of a major deletion in the SARS-CoV-2 genome on the severity of infection and the inflammatory response: an observational cohort study. *Lancet* **396**, 603–611 (2020).
- Carabelli, A. M. et al. SARS-CoV-2 variant biology: immune escape, transmission and fitness. *Nat. Rev. Microbiol.* **21**, 162–177 (2023).
- Pascall, D. J. et al. Inconsistent directions of change in case severity across successive SARS-CoV-2 variant waves suggests an unpredictable future. *medRxiv* <https://doi.org/10.1101/2022.03.24.22272915> (2022).
- Topol, E. J. High-performance medicine: the convergence of human and artificial intelligence. *Nat. Med.* **25**, 44–56 (2019).
- Steyaert, S. et al. Multimodal data fusion for cancer biomarker discovery with deep learning. *Nat. Mach. Intell.* **5**, 351–362 (2023).
- Steyaert, S. et al. Multimodal deep learning to predict prognosis in adult and pediatric brain tumors. *Commun. Med.* **3**, 44 (2023).
- Cheerla, A. & Gevaert, O. Deep learning with multimodal representation for pancancer prognosis prediction. *Bioinformatics* **35**, i446–i454 (2019).
- Hartmann, K., Sadée, C. Y., Satwah, I., Carrillo-Perez, F. & Gevaert, O. Imaging genomics: data fusion in uncovering disease heritability. *Trends Mol. Med.* **29**, 141–151 (2023).

19. Hutter, C. & Zenklusen, J. C. The Cancer Genome Atlas: creating lasting value beyond its data. *Cell* **173**, 283–285 (2018).
20. Shu, Y. & McCauley, J. GISAIID: global initiative on sharing all influenza data—from vision to reality. *Eur. Surveill.* **22**, 30494 (2017).
21. Hatcher, E. L. et al. Virus variation resource—improved response to emergent viral outbreaks. *Nucleic Acids Res.* **45**, D482–d490 (2017).
22. Ning, W. et al. Open resource of clinical data from patients with pneumonia for the prediction of COVID-19 outcomes via deep learning. *Nat. Biomed. Eng.* **4**, 1197–1207 (2020).
23. Hotelling, H. The most predictable criterion. *J. Educ. Psychol.* **26**, 139–142 (1935).
24. Witten, D. M., Tibshirani, R. & Hastie, T. A penalized matrix decomposition, with applications to sparse principal components and canonical correlation analysis. *Biostatistics* **10**, 515–534 (2009).
25. Ding, D. Y., Li, S., Narasimhan, B. & Tibshirani, R. Cooperative learning for multiview analysis. *Proc. Natl Acad. Sci. USA* **119**, e2202113119 (2022).
26. Hodcroft, E. B. CoVariants: SARS-CoV-2 mutations and variants of interest. (2021).
27. Kandeel, M., Mohamed, M. E. M., Abd El-Lateef, H. M., Venugopala, K. N. & El-Beltagi, H. S. Omicron variant genome evolution and phylogenetics. *J. Med. Virol.* **94**, 1627–1632 (2022).
28. Gruys, E., Toussaint, M. J., Niewold, T. A. & Koopmans, S. J. Acute phase reaction and acute phase proteins. *J. Zhejiang Univ. Sci. B* **6**, 1045–1056 (2005).
29. Simon, B. A., Christensen, G. E., Low, D. A. & Reinhardt, J. M. Computed tomography studies of lung mechanics. *Proc. Am. Thorac. Soc.* **2**, 517–521 (2005).
30. Çullu, N. et al. Efficacy of CT in diagnosis of transudates and exudates in patients with pleural effusion. *Diagn. Inter. Radiol.* **20**, 116–120 (2014).
31. Hie, B., Zhong, E. D., Berger, B. & Bryson, B. Learning the language of viral evolution and escape. *Science* **371**, 284–288 (2021).
32. Singh, R., Nagpal, S., Pinna, N. K. & Mande, S. S. Tracking mutational semantics of SARS-CoV-2 genomes. *Sci. Rep.* **12**, 15704 (2022).
33. Adjuik, T. A. & Ananey-Obiri, D. Word2vec neural model-based technique to generate protein vectors for combating COVID-19: a machine learning approach. *Int. J. Inf. Technol.* **14**, 3291–3299 (2022).
34. Nagpal, S. et al. Genomic surveillance of COVID-19 variants with language models and machine learning. *Front. Genet.* **13**, 858252 (2022).
35. Chen, W. et al. Machine learning with multimodal data for COVID-19. *Heliyon* **9**, e17934 (2023).
36. Xu, Q. et al. AI-based analysis of CT images for rapid triage of COVID-19 patients. *npj Digital Med.* **4**, 75 (2021).
37. Tomaszewski, M. R. & Gillies, R. J. The biological meaning of radiomic features. *Radiology* **298**, 505–516 (2021).
38. Zhou, M. et al. Non-small cell lung cancer radiogenomics map identifies relationships between molecular and imaging phenotypes with prognostic implications. *Radiology* **286**, 307–315 (2018).
39. Bartholomeus, G. A. et al. Robustness of pulmonary nodule radiomic features on computed tomography as a function of varying radiation dose levels—a multi-dose in vivo patient study. *Eur. Radiol.* **33**, 7044–7055 (2023).
40. Laino, M. E. et al. Prognostic findings for ICU admission in patients with COVID-19 pneumonia: baseline and follow-up chest CT and the added value of artificial intelligence. *Emerg. Radiol.* **29**, 243–262 (2022).
41. Zhao, K. et al. Defining dementia subtypes through neuropsychiatric symptom-linked brain connectivity patterns. *bioRxiv* <https://doi.org/10.1101/2023.07.02.547427> (2023).
42. Lee, H. et al. Multivariate association between brain function and eating disorders using sparse canonical correlation analysis. *PLoS ONE* **15**, e0237511 (2020).
43. Jameson, J. L. et al. *Harrison's Principles of Internal Medicine*, 20e (McGraw-Hill Education, 2018).
44. Mehta, P. et al. COVID-19: consider cytokine storm syndromes and immunosuppression. *Lancet* **395**, 1033–1034 (2020).
45. Levey, A. S. et al. Definition and classification of chronic kidney disease: a position statement from Kidney Disease: Improving Global Outcomes (KDIGO). *Kidney Int.* **67**, 2089–2100 (2005).
46. Newsome, P. N. et al. Guidelines on the management of abnormal liver blood tests. *Gut* **67**, 6–19 (2018).
47. Gong, K. et al. A multi-center study of COVID-19 patient prognosis using deep learning-based CT image analysis and electronic health records. *Eur. J. Radiol.* **139**, 109583 (2021).
48. Oi, Y. et al. Prediction of prognosis in patients with severe COVID-19 pneumonia using CT score by emergency physicians: a single-center retrospective study. *Sci. Rep.* **13**, 4045 (2023).
49. Butler, L. et al. Image and structured data analysis for prognostication of health outcomes in patients presenting to the ED during the COVID-19 pandemic. *Int. J. Med. Inf.* **158**, 104662 (2021).
50. Chao, H. et al. Integrative analysis for COVID-19 patient outcome prediction. *Med. Image Anal.* **67**, 101844 (2021).
51. Jiao, Z. et al. Prognostication of patients with COVID-19 using artificial intelligence based on chest x-rays and clinical data: a retrospective study. *Lancet Digit. Health* **3**, e286–e294 (2021).
52. Houldcroft, C. J., Beale, M. A. & Breuer, J. Clinical and biological insights from viral genome sequencing. *Nat. Rev. Microbiol.* **15**, 183–192 (2017).
53. Global Influenza Hospital Surveillance Network. <https://gihsn.org>.
54. Aksamentov, I., Roemer, C., Hodcroft, E. B. & Neher, R. A. Nextclade: clade assignment, mutation calling and quality control for viral genomes. *J. Open Source Softw.* **6**, 3773 (2021).
55. Kalyaanamoorthy, S., Minh, B. Q., Wong, T. K. F., von Haeseler, A. & Jermini, L. S. ModelFinder: fast model selection for accurate phylogenetic estimates. *Nat. Methods* **14**, 587–589 (2017).
56. Hoang, D. T., Chernomor, O., von Haeseler, A., Minh, B. Q. & Vinh, L. S. UFBoot2: improving the ultrafast bootstrap approximation. *Mol. Biol. Evol.* **35**, 518–522 (2017).
57. Nguyen, L.-T., Schmidt, H. A., von Haeseler, A. & Minh, B. Q. IQ-TREE: a fast and effective stochastic algorithm for estimating maximum-likelihood phylogenies. *Mol. Biol. Evol.* **32**, 268–274 (2014).
58. Yu, G. Using ggtree to visualize data on tree-like structures. *Curr. Protoc. Bioinforma.* **69**, e96 (2020).
59. Mikolov, T., Chen, K., Corrado, G. & Dean, J. Efficient estimation of word representations in vector space. *arXiv* <https://doi.org/10.48550/arXiv.1301.3781> (2013).
60. Zieleszinski, A., Vinga, S., Almeida, J. & Karlowski, W. M. Alignment-free sequence comparison: benefits, applications, and tools. *Genome Biol.* **18**, 186 (2017).
61. Nawaz, M. S. et al. Using alignment-free and pattern mining methods for SARS-CoV-2 genome analysis. *Appl. Intell.* **53**, 21920–21943 (2023).
62. Hadfield, J. et al. Nextstrain: real-time tracking of pathogen evolution. *Bioinformatics* **34**, 4121–4123 (2018).
63. Rambaut, A. et al. A dynamic nomenclature proposal for SARS-CoV-2 lineages to assist genomic epidemiology. *Nat. Microbiol.* **5**, 1403–1407 (2020).
64. Kuzmin, K. et al. Machine learning methods accurately predict host specificity of coronaviruses based on spike sequences alone. *Biochem. Biophys. Res. Commun.* **533**, 553–558 (2020).
65. Sokhansanj, B. A. & Rosen, G. L. Predicting COVID-19 disease severity from SARS-CoV-2 spike protein sequence by mixed effects machine learning. *Comput. Biol. Med.* **149**, 105969 (2022).
66. Mallory, J. D., Mallory, X. F., Kolomeisky, A. B. & Igoshin, O. A. Theoretical analysis reveals the cost and benefit of proofreading in coronavirus genome replication. *J. Phys. Chem. Lett.* **12**, 2691–2698 (2021).

67. Pedregosa, F. et al. Scikit-learn: machine learning in Python. *J. Mach. Learn. Res.* **12**, 2825–2830 (2011).
68. Fedorov, A. et al. 3D Slicer as an image computing platform for the Quantitative Imaging Network. *Magn. Reson. Imaging* **30**, 1323–1341 (2012).
69. Hofmanninger, J. et al. Automatic lung segmentation in routine imaging is primarily a data diversity problem, not a methodology problem. *Eur. Radiol. Exp.* **4**, 50 (2020).
70. van Griethuysen, J. J. M. et al. Computational radiomics system to decode the radiographic phenotype. *Cancer Res.* **77**, e104–e107 (2017).

Acknowledgements

This study was funded by the Foundation for Influenza Epidemiology and the Turkish Society of Internal Medicine. We gratefully acknowledge all data contributors, i.e., the Authors and their Originating laboratories responsible for obtaining the specimens and their Submitting laboratories for generating the genetic sequence and metadata and sharing via the GISAID Initiative, on which this research is based. A.G.E. gratefully acknowledges financial support for this project from the Fulbright Foreign Student Program, sponsored by the U.S. Department of State and the Turkish Fulbright Commission. Its contents are solely the author's responsibility and do not necessarily represent the official views of the Fulbright Program, the Government of the United States, or the Turkish Fulbright Commission. The research reported here was further supported by the National Cancer Institute (NCI) under award: R01 CA260271. The content is solely the authors' responsibility and does not necessarily represent the official views of the National Institutes of Health.

Author contributions

Conceptualization: A.G.E., M.D.T., Y.A.S., S.U. and O.G.; Methodology: A.G.E., D.Y.D., C.S. and O.G.; Collecting the data: A.G.E., B.E., M.U., M.C. and G.D.; Investigation: A.G.E., D.Y.D. and O.G.; Writing—original draft: A.G.E., D.Y.D. and O.G.; Writing—review & editing: A.G.E., D.Y.D., B.E.,

M.U., M.C., C.S., G.D., M.N.O., M.D.T., A.T., Y.A.S., R.T., S.U. and O.G.; Resources: M.D.T., S.U. and O.G.; Supervision: O.G.

Competing interests

The authors declare no competing interests.

Additional information

Supplementary information The online version contains supplementary material available at <https://doi.org/10.1038/s41746-024-01128-2>.

Correspondence and requests for materials should be addressed to Ahmet Gorkem Er or Olivier Gevaert.

Reprints and permissions information is available at <http://www.nature.com/reprints>

Publisher's note Springer Nature remains neutral with regard to jurisdictional claims in published maps and institutional affiliations.

Open Access This article is licensed under a Creative Commons Attribution 4.0 International License, which permits use, sharing, adaptation, distribution and reproduction in any medium or format, as long as you give appropriate credit to the original author(s) and the source, provide a link to the Creative Commons licence, and indicate if changes were made. The images or other third party material in this article are included in the article's Creative Commons licence, unless indicated otherwise in a credit line to the material. If material is not included in the article's Creative Commons licence and your intended use is not permitted by statutory regulation or exceeds the permitted use, you will need to obtain permission directly from the copyright holder. To view a copy of this licence, visit <http://creativecommons.org/licenses/by/4.0/>.

© The Author(s) 2024

¹Stanford Center for Biomedical Informatics Research (BMIR), Department of Medicine, Stanford University, Stanford, CA 94305, USA. ²Department of Health Informatics, Graduate School of Informatics, Middle East Technical University, 06800 Ankara, Turkey. ³Department of Infectious Diseases and Clinical Microbiology, Hacettepe University Faculty of Medicine, 06230 Ankara, Turkey. ⁴Department of Biomedical Data Science, Stanford University, Stanford, CA 94305, USA. ⁵Department of Internal Medicine, Division of Intensive Care Medicine, Hacettepe University Faculty of Medicine, 06230 Ankara, Turkey. ⁶Department of Internal Medicine, Hacettepe University Faculty of Medicine, 06230 Ankara, Turkey. ⁷Department of Radiology, Hacettepe University Faculty of Medicine, 06230 Ankara, Turkey. ⁸Department of Statistics, Stanford University, Stanford, CA 94305, USA. ✉e-mail: ahmetgorkemer@gmail.com; ogevaert@stanford.edu